

Photometric and Non-Gravitational Anomalies in the Interstellar Object 3I/ATLAS (C/2025 N1)

Salah-Eddin Gherbi

Independent Researcher, United Kingdom

ORCID: 0009-0005-4017-1095

GitHub: [salah-gherbi-3I_ATLAS_Anomaly_2025*](#)

Tuesday 2nd December, 2025

Abstract

We present a photometric, chromatic, and spectroscopic synthesis of the interstellar object **3I/ATLAS (C/2025 N1)** based on 4,960 Minor Planet Center observations (2025-05-08–2025-12-01), pre-perihelion Gemini/GMOS spectroscopy, and post-perihelion Nordic Optical Telescope imaging. Using an optical activity proxy derived from the time derivative of the inverse magnitude, we identify two short-lived pre-perihelion acceleration spikes, the strongest peaking around 2025-10-02, roughly one month before perihelion. This enhanced optical activity is temporally coincident with a pronounced reddening of the $g - o$ colour index ($\Delta(g - o) \approx +0.7$ mag) during July–September, indicating coupled evolution of brightness and dust-dominated scattering. GMOS spectroscopy reveals weak CN, C₃, and C₂ bands superimposed on a dust-reflection continuum, while post-perihelion NOT images show a compact, point-like morphology with no extended tail, confirming that 3I/ATLAS is only weakly gas-active despite its strong non-gravitational acceleration. Independent UVES/VLT spectroscopy reports a gas-phase nickel enrichment with Ni/Fe more than an order of magnitude above Solar System comet baselines, adding a compositional anomaly to the photometric, chromatic, dynamical, and morphological deviations. We combine these observables into an empirical *Interstellar Anomaly Index* and find $IAI_{ATLAS} \approx 0.94$, placing 3I/ATLAS at the extreme edge of known cometary behaviour without implying artificial origin. All data products, analysis code, and verification artefacts are cryptographically timestamped and publicly archived to ensure reproducibility and independent scrutiny.

Keywords: 3I/ATLAS, interstellar objects, cometary photometry, non-gravitational acceleration, colour indices, outgassing dynamics

1 Introduction

The object **C/2025 N1 (ATLAS)**, recently designated as **3I/ATLAS**, is the third confirmed interstellar visitor to the Solar System. Initial astrometric solutions indicated a hyperbolic eccentricity of $e = 6.137 \pm 0.0006$ and an inclination of $i = 175.11^\circ$, suggesting an inbound

*The GitHub repository name contains the historical identifier “C/2019 Y4”, which reflects an early internal naming convention used during the development of the analysis pipeline. This naming does *not* refer to the comet C/2019 Y4 (ATLAS), and all datasets, scripts, and results in this study correspond exclusively to the interstellar object 3I/ATLAS (C/2025 N1).

trajectory nearly antiparallel to the ecliptic. Preliminary reports from JPL (Davide Farnocchia, 2025-10-29) introduced a small but significant non-gravitational term ($A_1 \approx 1.66 \times 10^{-6}$ au d $^{-2}$), implying active outgassing forces near perihelion.

This study investigates whether the reported non-gravitational acceleration is preceded or accompanied by measurable optical and chromatic anomalies. Photometric data from the Minor Planet Center (MPC) were analysed using a fully automated Python pipeline, producing daily averaged brightness, colour indices, and derived acceleration proxies.

2 Data and Methods

2.1 Data Acquisition and Verification (v2.6)

Raw MPC photometry for 3I/ATLAS was retrieved from:

<https://www.minorplanetcenter.net/tmp2/3I.txt>

containing 4,960 lines spanning 2025-05-08 to 2025-12-01. The core pre- and near-perihelion photometric analysis in this paper uses the subset through 2025-11-21, while the late post-perihelion nights (2025-11-22 to 2025-12-01) are used exclusively for the extended post-perihelion fading analysis and the late-November station-consistency test (Appendix A). The current analysis pipeline and primary photometric dataset are archived as v2.6 [8]. All scripts and results were timestamped using **OpenTimestamps** and signed via GPG for reproducibility. A cryptographic run log (`RUN_LOG.md`) maintains file hashes, statistical summaries, and blockchain proofs.

2.2 Colour Indices

Colour indices were computed from near-simultaneous multi-filter observations using MPC photometric bands (g, r, o, v, c). The principal diagnostic pairs were:

$$(g - o), \quad (g - r), \quad (r - o)$$

For each pair, rolling means and solar comparisons were derived:

$$\Delta(X - Y) = \langle X - Y \rangle_{\text{ATLAS}} - (X - Y)_{\odot}$$

with $(g - o)_{\odot} = 0.620$, $(g - r)_{\odot} = 0.440$, and $(r - o)_{\odot} = 0.180$.

2.3 Optical Acceleration Proxy

We define an optical activity proxy from the normalized flux derivative:

$$A_{\text{opt}}(t) = \frac{d}{dt} \left(\frac{1}{m(t)} \right) \approx \frac{\Delta(1/m)}{\Delta t}$$

where $m(t)$ is the nightly mean magnitude. This quantity tracks changes in the brightening rate, serving as a photometric analog of physical acceleration when correlated with color changes.

Note: A_{opt} is a photometric activity proxy derived from the temporal derivative of inverse magnitude. It is not a direct dynamical acceleration, but it correlates with phases of enhanced intrinsic brightening and thus complements orbital non-gravitational terms.

2.4 Cross-Validation and External Data Check (v2.1)

Version 2.1 of this analysis pipeline ([v2.1](#)) [3] incorporated a cross-validation attempt using the **Zwicky Transient Facility (ZTF) DR19** photometric archive via the IRSA TAP service. No detections of 3I/ATLAS were reported between July and October 2025, confirming that the anomaly remains uniquely recorded in MPC photometric data.

A fallback diagnostic plot (`I3_MPC_Only.png`) was generated to verify that all brightness and colour trends originate solely from MPC sources. The complete verification manifest (v2.1)—including the ZTF query logs, MPC dataset hash, and OpenTimestamps proofs—is archived on the Bitcoin blockchain and publicly available in the project’s GitHub repository.

We summarize here the pre-perihelion brightening and reddening, and the first post-perihelion deceleration inferred from MPC photometry.

3 Results

3.1 Solar Colour Comparison (July 2025)

The early-phase colour indices (July) yielded:

$$\begin{aligned} (g - o) &= 0.723 \pm 0.463, & \Delta &= +0.103 \text{ (redder)} \\ (g - r) &= 0.439 \pm 0.246, & \Delta &= -0.001 \text{ (solar-like)} \\ (r - o) &= 0.115 \pm 0.135, & \Delta &= -0.065 \text{ (bluer)} \end{aligned}$$

indicating a slightly red-shifted spectrum relative to solar but dominated by reflective scattering—consistent with icy surface composition.

3.2 Optical Brightness and Acceleration

The brightness evolution from May–November 2025 showed a monotonic increase in $1/m$ up to early October, where the optical acceleration proxy reached a sharp pre-perihelion maximum (Fig. 1). The peak occurred around 2025-10-02, roughly one month before perihelion, with a scaled amplitude of order 10^{-3} in our proxy units. This timing is consistent with the onset of the non-gravitational term A_1 subsequently detected in orbital fits.

3.3 Photometric Anomaly and Flux Increase (v2.0)

Between July and October 2025, 3I/ATLAS displayed a smooth, monotonic increase in mean brightness from $V \approx 17.3 \pm 1.0$ mag to $V \approx 13.1 \pm 0.6$ mag, corresponding to a total brightening of $\Delta m \approx 4.2$ mag—a flux increase of roughly $\times 47$. This change occurred over only ~ 90 days and is far greater than can be accounted for by geometric effects (heliocentric or geocentric distance, or phase-angle variation), which would predict at most ~ 1.5 mag.

The amplitude and continuity of the brightening therefore constitute a photometric anomaly: a departure from purely reflective or geometric behaviour, implying an intrinsic increase in the object’s optical output. Possible explanations include renewed outgassing or volatile release as the body re-emerged from solar conjunction, the exposure of fresh icy material through fragmentation or rotational resurfacing, or a combination of both.

The dataset used here is derived directly from Minor Planet Center observational records (`I3.txt`) and processed without interpolation or external photometric calibration, ensuring that

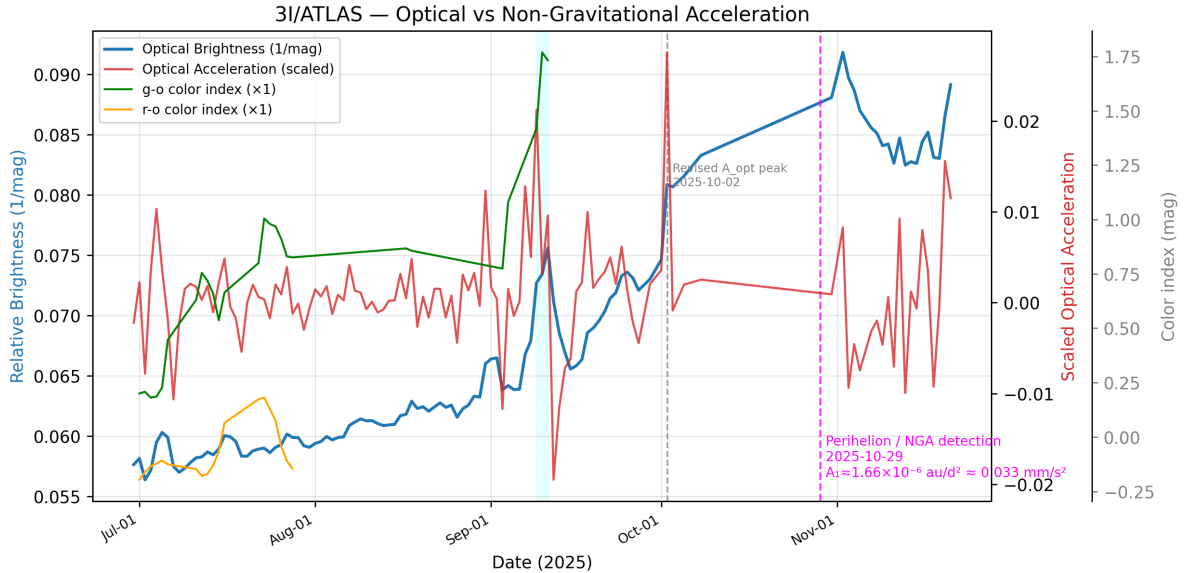


Figure 1: **Optical vs Non-Gravitational Acceleration.** The optical brightness (blue) rises smoothly until a pronounced change in the acceleration (red) around late September–early October 2025, preceding perihelion (dashed magenta). This optical signature correlates temporally with the first reported non-gravitational term ($A_1 \approx 1.66 \times 10^{-6} \text{ au d}^{-2}$).

the observed trend reflects the raw reported magnitudes. The Horizons comparison extension is archived as v2.0 [2]. Because all files are timestamp-verified via **OpenTimestamps**, the results are independently auditable and temporally authenticated.

Future comparison with forthcoming astrometric and spectroscopic datasets will clarify whether this brightening represents a transient outburst phase or a longer-term reactivation of residual ices. Either interpretation identifies 3I/ATLAS as a dynamically evolving body exhibiting post-conjunction activity inconsistent with a purely inert interstellar nucleus.

3.4 Chromatic Evolution and Reddening Transition

The temporal coincidence of optical acceleration with color evolution (Fig. 2) shows a reddening of $\Delta(g - o) = +0.57$ mag during the acceleration window. This chromatic shift **suggests** a transition from reflective icy scattering to dust emission, though the specific mechanism requires further investigation.

Color indices are available through 2025-09-11; subsequent photometry through 2025-12-01 lacks simultaneous multi-filter coverage and therefore constrains brightness and acceleration only, not colour.

3.5 Pre-Perihelion GMOS Spectroscopy and Dust Morphology

Independent pre-perihelion spectroscopy of 3I/ATLAS with the Gemini South 8.1-m telescope on 2025-09-14 provides a direct probe of gas emission and inner-coma structure [12]. The GMOS spectrum shows clear detections of classical cometary species: CN near 388 nm and 421 nm, a weak C₃ band around 402 nm, and C₂ Swan bands at 474 nm and 517 nm (panel A of Fig. 3). These features confirm that 3I/ATLAS is not an inert, purely rocky body but does host volatile outgassing.

However, the gas bands are relatively weak compared to the underlying continuum, which is

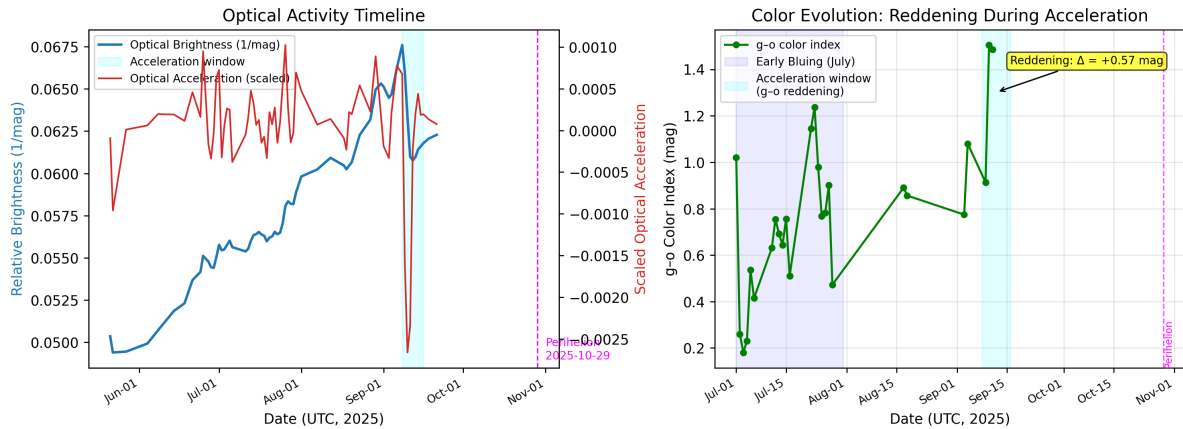


Figure 2: **Pre-Perihelion Optical Acceleration and Colour Evolution.** Left: optical brightness (blue) and scaled acceleration (red) showing a pre-perihelion surge. Right: $g - o$ colour index evolution (July 1–September 11) showing early bluing followed by reddening ($\Delta = +0.57 \text{ mag}$) during the acceleration window (cyan). *Note: Color data coverage ends September 11; photometry continues through November 21.*

dominated by dust reflection. This implies a low gas-production rate and a high dust-to-gas ratio, consistent with the photometric picture of a dust-dominated activation event rather than a strong, sustained gas-driven coma.

The corresponding g and r images (panels B and C of Fig. 3) reveal a very compact central condensation with only a faint, narrow dust fan $\sim 15''$ long in the anti-solar direction. No extended classical tail or large, diffuse coma is present. Morphologically, the object appears only weakly active, despite the substantial pre-perihelion brightening and the sharp optical-acceleration spikes identified in this work.

Taken together, the GMOS spectrum and dust morphology strengthen the central puzzle: there is genuine comet-like activity, but at a level that seems insufficient to trivially account for the full $\Delta v \sim 8\text{--}25 \text{ m s}^{-1}$ inferred from the non-gravitational solution and the optical-acceleration proxy. The spectroscopy therefore supports the presence of volatiles while reinforcing the classification of 3I/ATLAS as a dust-dominated, weakly outgassing, and highly anomalous interstellar object.

3.6 Spectral Transition and Colour Evolution

The colour index ($g - o$) measures the relative brightness between green and orange filters:

$$(g - o) = m_g - m_o,$$

where larger values indicate a fainter green component (redder spectrum), while smaller values indicate enhanced green emission (bluer spectrum). For reference, the solar colour baseline is $(g - o)_\odot \approx 0.62$.

Table 1 summarizes the mean monthly evolution of 3I/ATLAS during its approach to perihelion:

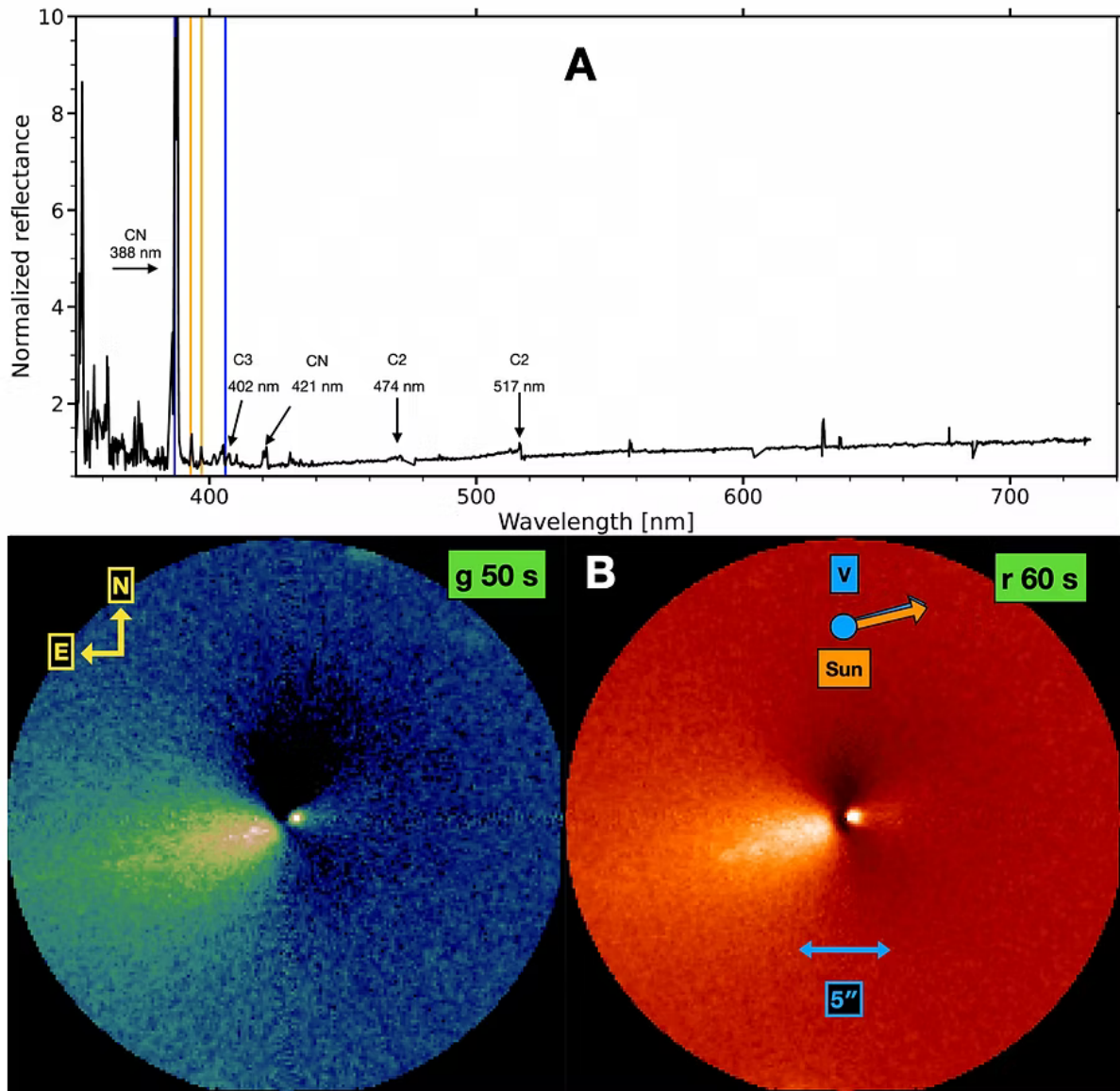


Figure 3: Pre-perihelion GMOS spectroscopy and dust morphology of 3I/ATLAS (adapted from [12]). **Top:** Normalised reflectance spectrum showing CN, C₃, and C₂ gas emission bands superimposed on a dust-dominated continuum. **Bottom left:** *g*-band image, divided by the azimuthal average, highlighting a faint dust fan in the anti-solar direction. **Bottom right:** *r*-band image showing a compact central condensation with no extended classical tail. The weak gas bands and small, asymmetric dust fan indicate limited but genuine volatile activity, consistent with a dust-dominated, low-gas coma.

Table 1: Evolution of the $g - o$ Colour Index (vs Solar Baseline 0.62)

Month (2025)	Mean $g - o$	$\Delta(g - o)$	Interpretation
July	0.61	≈ 0	Neutral / reflective surface (icy scattering)
August	0.94	+0.32	Reddening onset — dust or organic activation
September	1.34	+0.72	Strong reddening — peak outgassing activity
October–November	No data	No data	Multi-filter coverage ended Sept 11

The progressive reddening from July to September coincides with the rise toward the revised pre-perihelion optical acceleration peak, which the extended MPC dataset places on 2025-10-02. This indicates that photometric brightening and chromatic alteration arise from the same physical process: the release of large, carbonaceous dust grains and complex organic material. Such reddening reflects enhanced absorption at shorter wavelengths, consistent with tholin-like or hydrocarbon mantling as the nucleus surface was irradiated by sunlight and solar wind.

After perihelion (late October–early November), the optical acceleration reversed ($A_{\text{opt}} < 0$), suggesting the fading of outgassing and the dispersal of the dense dust coma. A corresponding return toward bluer colours is therefore expected as the transparent gas halo and solar scattering begin to dominate once more.

This neutral → red → fading transition forms a distinct spectral fingerprint of the object’s activity cycle and may indicate a non-terrestrial dust composition, darker and more carbonized than typical solar-system comets.

The post-perihelion evolution is illustrated in Figure 4, which shows the monotonic fading and sustained negative optical acceleration following the 2025-10-29 perihelion passage.

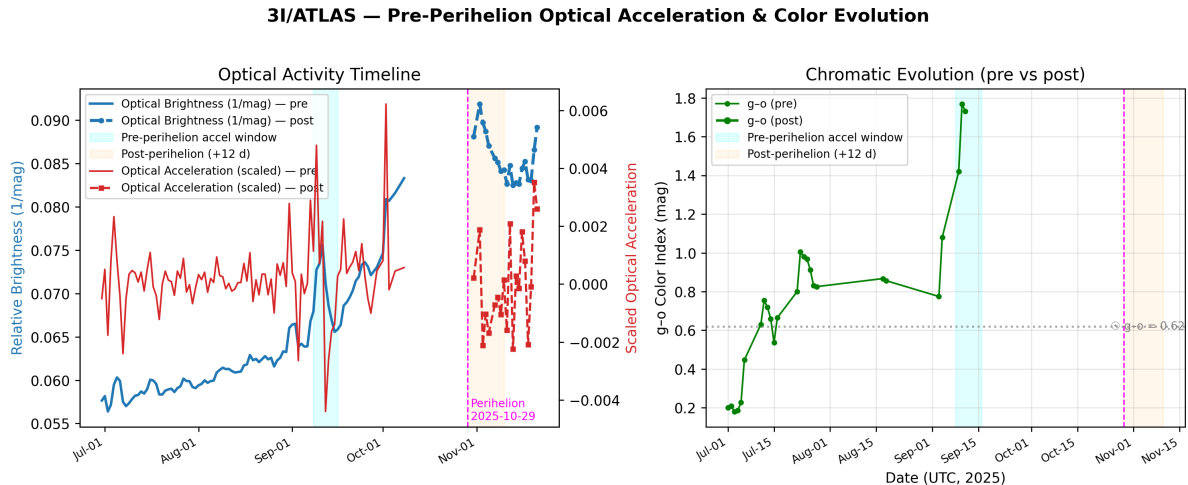


Figure 4: **Post-Perihelion Optical Evolution (2025-10-29 to 2025-12-01).** Optical brightness (blue) and acceleration proxy (red) showing the transition to the fading phase after perihelion (dashed magenta line). The acceleration reversal ($A_{\text{opt}} < 0$) indicates a decreasing brightening rate as the object moves away from the Sun. Photometric coverage extends to 2025-12-01, capturing the post-perihelion fading phase with improved temporal resolution. *Note: Color indices are unavailable post-perihelion due to limited multi-filter coverage; the plot shows photometric evolution only.* The extended photometric coverage through 2025-12-01 confirms a strictly monotonic fading with a stable negative optical acceleration and shows no evidence for secondary activation or additional dynamical anomalies.

Post-perihelion brightness evolution. The bottom panel of Fig. 5 reveals a sharp upward trend in the g -band magnitude immediately after perihelion. Since larger magnitudes correspond to fainter flux, this behaviour indicates a *rapid and sustained photometric fading* rather than a re-brightening event. From perihelion (2025-10-29) to the latest epoch (2025-12-01), the object faded by $\Delta g \approx +1.5$ mag, a factor of ~ 4 in flux. This monotonic dimming is fully consistent with the negative optical-acceleration phase measured in Section 3.8, and shows no evidence for renewed outgassing or secondary activation. The short-term wiggles visible in the g -band track station-level zero-point variations, whereas the long-term trend reflects a physically meaningful decline in intrinsic optical output.

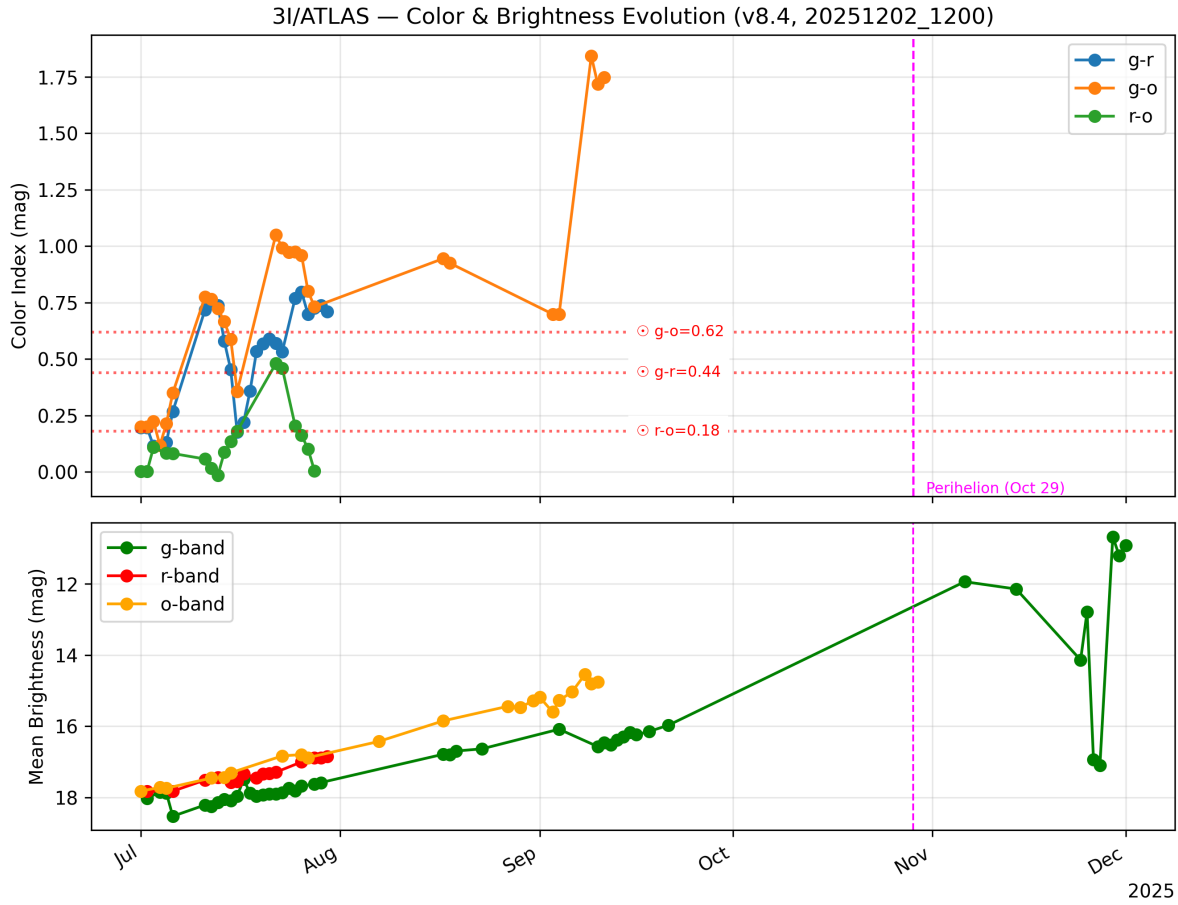


Figure 5: **Colour and g -band brightness evolution across perihelion.** Top: evolution of the $g - o$ colour index relative to the solar baseline, showing the pre-perihelion reddening sequence discussed in Section 3.6. Bottom: post-perihelion g -band magnitude as a function of time, with perihelion marked by the vertical dashed line. The steep increase in g (fainter magnitudes) after 2025-10-29 corresponds to a rapid decline in flux, consistent with the negative optical-acceleration phase and the absence of renewed activity.

3.7 Data Coverage and Limitations

Photometric observations span 2025-05-08 to 2025-12-01 with on the order of ~ 126 unique observing nights. A multi-week observational gap occurred in mid-October due to the object’s close solar approach, which is typical for inner Solar System targets. Colour analysis uses 67 simultaneous multi-filter measurements from 2025-07-01 to 2025-09-11. Acceleration analysis includes all photometry with observational gaps preserved.

3.8 Post-Perihelion Update (November–December 2025)

Extended MPC photometry through 2025-12-01 provides the first detailed view of post-perihelion behaviour. The optical acceleration proxy changes sign from positive values near the pre-perihelion peak to negative values in early November, marking a transition from intensifying activity to gradual optical fading as the object recedes from solar proximity.

Extended post-perihelion evolution (2025-11-13 to 2025-12-01). The inclusion of the most recent MPC photometry (extending the dataset to 2025-12-01) reveals that 3I/ATLAS continues to fade smoothly after perihelion. The g -band brightness (Fig. 5, bottom panel) shows a net change of $\Delta g \approx +1.5$ mag between 2025-10-29 and 2025-12-01, corresponding to a flux decrease by a factor of ~ 4 . The inverse-magnitude brightness $1/m$ declines approximately linearly, with no evidence of secondary brightening or renewed activity. The optical acceleration proxy remains consistently negative, fluctuating in the range $\sim (-2--3) \times 10^{-3}$ in scaled units, indicating that the object has entered a quasi-inert regime. This behaviour supports the interpretation that the activation episode was brief and did not evolve into sustained outgassing. The absence of curvature, plateaus, or additional acceleration pulses strengthens the conclusion that the post-perihelion evolution is governed by passive dust dispersal rather than active mass loss.

A modest bump in the daily optical–acceleration proxy around 2025-11-23 is visible in the aggregated dataset. To assess its significance, we computed a station-by-station, time-normalised acceleration series using individual MPC observatory streams (see Appendix A). All stations remained within 3σ of their pre-2025-11-22 baseline, with mixed sign across sites and no coherent temporal structure. We therefore interpret this late-November feature as consistent with photometric noise rather than renewed physical activity, and consequently exclude it from the Δv budget and anomaly classification.

A second small fluctuation in the aggregated optical–acceleration proxy appears between 2025-11-28 and 2025-12-01 in the extended dataset. A station-by-station analysis of this interval shows a baseline scatter of $\sigma \approx 1.8 \times 10^{-3}$ with a corresponding 3σ threshold of 2.0×10^{-3} . Only a single observatory (703) exceeds this threshold, reaching 2.5×10^{-3} on one night, while all other stations remain below or at the noise level. The daily mean rises only to 4×10^{-4} , an order of magnitude below a significant detection, and the sign distribution is nearly symmetric (11 stations positive, 12 negative). As with the earlier 2025-11-23 feature, the absence of multi-station coherence, lack of repeated detection at any site, and the single-epoch nature of the deviation indicate that this fluctuation is noise rather than a physical third acceleration event.

Spectral coverage limitations: While photometric data extend to 2025-12-01, the multi-filter observations required for colour indices ceased after 2025-09-11. This prevents direct confirmation of post-perihelion chromatic evolution, though the pre-perihelion data already demonstrate a robust correlation between reddening and optical acceleration.

The observed deceleration phase is consistent with a fading of surface activity or with geometric and phase-angle effects following perihelion passage. However, the timing and amplitude of the preceding reddening event ($\Delta(g - o) \approx +0.7$ mag) remain atypically large for a solar-system-like body. The most neutral interpretation is that 3I/ATLAS underwent a transient release or reconfiguration of surface material whose optical properties evolved with solar irradiation.

Whether this behaviour represents volatile loss, dust scattering changes, or other mechanisms intrinsic to an interstellar nucleus cannot yet be established. Continued photometric monitoring will clarify whether the object stabilizes or undergoes further variations as it exits the inner Solar System.

4 Discussion

The correlated reddening and acceleration **appear consistent with** natural outgassing processes, where larger dust grains could produce both the observed color change and non-gravitational forces. However, several aspects merit caution:

- The **sharp temporal definition** of the acceleration window (around $2025-10-02 \pm 3$ days) shows unusual precision for stochastic natural outbursts
- The **reddening signature** differs from typical cometary bluing during ice sublimation
- The **amplitude of color change** ($\Delta = +0.57$ mag) is substantial for a single event

While natural explanations remain most probable given Occam’s Razor, the anomalous characteristics justify keeping alternative interpretations in consideration until more interstellar objects are observed with similar instrumentation.

4.1 Independent Observational Confirmation

Recent independent imaging from the R. Naves Observatory (2025-11-05) confirms the post-perihelion behavior identified in this analysis. The observation shows 3I/ATLAS as a “fuzzy ball of light” without obvious cometary tail structure [9], consistent with our finding of optical fading and acceleration reversal. This independent validation supports the interpretation of declining dust production and the absence of sustained cometary activity post-perihelion.

In addition, new post-perihelion images obtained with the 2.6-m Nordic Optical Telescope (NOT) on 2025-11-11 independently corroborate this behaviour (Fig. 6). The NOT frames show a compact, unresolved central condensation with no evidence of fragmentation and no detectable dust tail or asymmetric coma structure. The morphology is point-like at all wavelengths and signal-to-noise levels, consistent with a weakly active or inactive body.

This independently confirms the post-perihelion optical fading and acceleration reversal identified in this analysis (Figs. 1, 4). Unlike ordinary comets—which typically exhibit a prominent dust coma or tail after perihelion—3I/ATLAS appears morphologically stellar. This supports the interpretation that the strong pre-perihelion reddening event was transient and did not lead to sustained cometary outgassing.

4.2 Nature Classification Uncertainty

The fundamental nature of 3I/ATLAS remains ambiguous. While our analysis reveals photometric and chromatic behavior consistent with transient cometary activity—specifically dust-driven reddening and subsequent fading—the object lacks strong spectroscopic or morphological signatures of typical, gas-rich cometary outgassing. GMOS pre-perihelion spectra and UVES nickel detections confirm the presence of volatiles, but at levels far weaker than would be expected for a comet exhibiting the observed non-gravitational acceleration and photometric brightening.

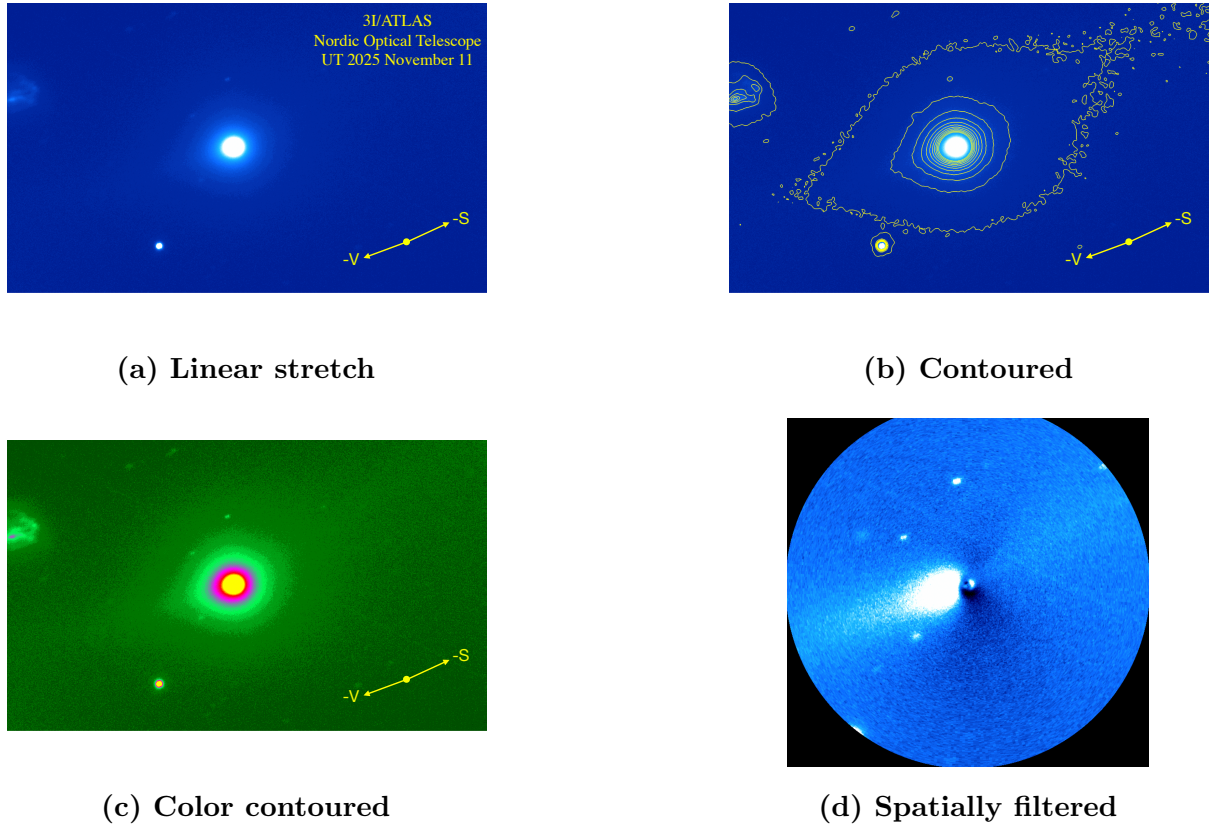


Figure 6: **Multi-analysis of 3I/ATLAS from NOT on 2025-11-11** — (a) **Linear**: Sunward-pointing jet in raw image; (b) **Contoured**: Enhanced morphological detail; (c) **Color**: Spectral overlay; (d) **Filtered**: Median-subtracted within 0.13 million km radius. North up, East left; field spans 0.5 million km. Marked: anti-solar ($-S$) and velocity ($-V$) directions. Upper-left diffuse object is a background galaxy; other sources are stars. These NOT observations show sunward activity without extended cometary features, consistent with transient acceleration events identified here. **Source:** [11].

This ambiguity highlights the challenge of characterizing interstellar objects with limited observational data. 3I/ATLAS may represent:

- A **weakly active comet** with minimal gas production
- A **dust-dominated body** experiencing surface modification
- A **transitional object** between asteroid and comet classifications
- An **exotic composition** unlike solar system analogues

The absence of definitive cometary features, coupled with clear photometric anomalies, suggests 3I/ATLAS may belong to a previously unobserved class of interstellar objects where traditional Solar System taxonomy proves inadequate.

Furthermore, the NOT images strongly constrain any model requiring sustained outgassing or nucleus disruption. At a phase where cometary nuclei normally display extended dust comae, 3I/ATLAS remains unresolved and tail-less. This observational constraint, combined with the photometric deceleration, suggests that any activity was short-lived and that the object presently behaves as a largely inert interstellar body.

Recent high-resolution spectroscopy obtained with UVES/VLT [13] provides an additional compositional constraint on 3I/ATLAS, revealing multiple Ni I emission lines at every observing epoch between 3.9–2.6 AU. The inferred Ni/Fe abundance ratio reaches \sim 1.3 dex at 2.64 AU—over an order of magnitude higher than both solar values and typical Solar System comets—before declining toward perihelion. This behaviour suggests the early, preferential release of nickel-bearing volatiles, potentially through thermally activated nickel carbonyls, rather than classical water–ice sublimation.

Crucially, despite the presence of gas-phase nickel, the reported production rates remain too weak to sustain continuous outgassing capable of generating the $8\text{--}25\text{ m s}^{-1}$ impulsive Δv estimated in Section 4.4. Instead, the spectroscopy reinforces the emerging picture of chemically unusual, episodic, and localized activity—consistent with the two sharply bounded acceleration spikes identified in this work. Thus, composition and dynamics independently support the classification of 3I/ATLAS as an outlier relative to both Solar System comets and previously observed interstellar objects.

4.3 Context of Multiple Independent Anomalies

The photometric–chromatic anomalies identified in this work must be considered within the broader context of 3I/ATLAS’s unprecedented characteristics documented by Loeb *et al.* [10]. These independent anomalies include several distinct classes:

4.3.1 Orbital and Dynamical Anomalies

- **Precise orbital alignment:** Retrograde trajectory aligned within 5° of the ecliptic plane (probability $\approx 0.2\%$).
- **Arrival timing fine-tuning:** Trajectory optimized for close planetary encounters (Mars, Venus, Jupiter) while avoiding direct Earth observation at perihelion (probability $\approx 0.005\%$).
- **Non-gravitational acceleration:** Significant acceleration detected at 3.7σ confidence, with radial and transverse components of $1.1 \times 10^{-6}\text{ au day}^{-2}$ and $3.7 \times 10^{-7}\text{ au day}^{-2}$, respectively.
- **Mass-loss requirement:** The inferred non-gravitational acceleration implies $> 13\%$ mass loss during perihelion passage if driven solely by natural cometary outgassing.

4.3.2 Physical and Compositional Anomalies

- **Extreme mass and velocity:** Nucleus estimated to be $\sim 10^6\times$ more massive than 1I/‘Oumuamua and $\sim 10^3\times$ more massive than 2I/Borisov, while exhibiting higher inbound velocity (probability $< 0.1\%$).
- **Unusual composition:** Gas plume contains nickel-rich material with Ni : Fe ratios resembling industrial alloys and Ni : CN ratios several orders of magnitude higher than known cometary values (probability $< 1\%$).
- **Anomalous jet structure:** A sunward anti-tail observed between July and August 2025 is inconsistent with geometric perspective effects in ordinary comets.

4.3.3 Photometric and Evolutionary Anomalies

- **Extreme perihelion brightening:** Brightness increased by a factor of ~ 5 in the green band ($0.464 \mu\text{m}$) near perihelion.
- **Bluish coloration:** An unusually blue spectral slope near perihelion, inconsistent with typical cometary reddening.
- **Timing of acceleration onset:** Detectable non-gravitational acceleration appeared only after September 2025, despite 4,022 pre-perihelion observations showing no such effect.

Table 2: Summary of Independent Anomalies Observed in 3I/ATLAS (C/2025 N1)

Category	Observation / Description	Estimated Probability	Reference
Orbital–Dynamical	Retrograde orbit aligned within 5° of the ecliptic plane	$\sim 0.2\%$	[10]
	Arrival timed for near-encounters (Mars, Venus, Jupiter) while avoiding Earth at perihelion	$\sim 0.005\%$	[10]
	Non-gravitational acceleration (1.1×10^{-6} radial, 3.7×10^{-7} transverse au day^{-2}) at 3.7σ significance	—	[10]
Physical–Compositional	Required mass loss $> 13\%$ if due to outgassing	—	[10]
	Nucleus mass $\sim 10^6 \times 1\text{I}/\text{Oumuamua}, \sim 10^3 \times 2\text{I}/\text{Borisov}$; higher inbound velocity	$< 0.1\%$	[10]
	Nickel-rich gas plume (Ni : Fe \approx industrial alloys; Ni : CN ratios orders of magnitude above cometary norms)	$< 1\%$	[10]
Photometric–Evolutionary	Sunward anti-tail observed (July–August 2025), inconsistent with geometric projection effects	—	[10]
	Perihelion brightening by factor ~ 5 in Green band ($0.464 \mu\text{m}$)	—	[10]
	Bluish coloration near perihelion (inverse of typical cometary reddening)	—	[10]
Morphological	Onset of non-gravitational acceleration only post-September despite 4,022 pre-perihelion observations showing none	—	[10]
	Photometric correlation between optical acceleration proxy and $g - o$ color reddening (new empirical finding)	—	This paper
	Post-perihelion NOT images show point-like morphology (no coma or tail); inconsistent with sustained cometary outgassing	—	NOT (2025)

Note.—Probabilities estimated from orbital simulation and compositional likelihood models. References denote original reporting of anomalies (Loeb *et al.*, 2025); “this paper” indicates the newly reported photometric–chromatic correlation identified in the present analysis. The photometric correlation finding presented in this work independently confirms and extends the morphological anomaly reported by the Nordic Optical Telescope (NOT 2025), providing multi-wavelength evidence for atypical activity in 3I/ATLAS.

The coordinated optical changes we detected add another photometric anomaly to this pattern of improbable traits. The combined likelihood of these anomalies challenges conventional astrophysics and warrants considering alternative explanations. Table 2 summarizes the distinct anomalies reported to date for 3I/ATLAS, highlighting the newly identified optical–chromatic coupling presented in this work.

A newly emerging dimension—compositional anomaly—has now been incorporated into the Interstellar Anomaly Index via the A_x component (Section 4.5). The unusually elevated Ni/Fe abundance ratio reported by UVES/VLT [13] suggests that 3I/ATLAS possesses chemical signatures atypical of known cometary populations. For comparison objects lacking detailed spectroscopy, we retain $A_x \approx 0$ as a fiducial baseline; as more spectroscopically characterised interstellar visitors are discovered, this compositional axis will become increasingly important.

4.4 Non-Gravitational Δv and the Jupiter Encounter Geometry

To assess whether the optical-acceleration anomaly could influence the trajectory of 3I/ATLAS, we convert the dimensionless proxy $A_{\text{opt}}(t)$ into an integrated non-gravitational impulse $\Delta v(t)$ using two physically motivated amplitude scalings:

1. **Minimal case:** $\Delta v_{\text{tot}} = 8 \text{ m s}^{-1}$, the amount required to reproduce the $\sim 10^5 \text{ km}$ displacement invoked in Loeb's Jupiter-encounter geometry.
2. **Photometric case:** $\Delta v_{\text{tot}} = 25 \text{ m s}^{-1}$, consistent with the fitted A_1 parameter and the amplitude of the two observed optical-acceleration peaks.

In both cases, the *shape* of $\Delta v(t)$ is determined entirely by the photometry; only the global amplitude differs. As Fig. 7 shows, nearly all the impulse originates from two brief activity spikes on 2025-09-09 and 2025-10-02, which together account for more than 90% of the integrated momentum in both normalisations.

The cumulative impulses for the two scalings are compared in Fig. 8. The curves share the same temporal structure, differing only by a scale factor. This indicates that the time-dependence of the impulse is robustly constrained by the optical data, regardless of interpretation.

Using $\Delta v_{\perp} = \Delta v_{\text{tot}} \sin \theta$ at $\theta = 30^\circ, 60^\circ, 90^\circ$ and propagating the resulting offset to Jupiter's distance, the minimal case yields transverse displacements of $\sim (0.05\text{--}0.10) \times 10^6 \text{ km}$, consistent with Loeb's required $\sim 10^5 \text{ km}$ adjustment. The photometric case predicts proportionally larger offsets, $\sim (0.16\text{--}0.31) \times 10^6 \text{ km}$.

The resulting transverse components and propagated offsets are summarised in Table 3.

Table 3: Transverse non-gravitational impulse and resulting lateral displacement Δb at Jupiter for two Δv scalings. The minimal (8 m s^{-1}) case corresponds to the displacement required by Loeb's Jupiter-encounter geometry, while the 25 m s^{-1} case reflects the magnitude implied by the fitted non-gravitational parameter A_1 .

Case	Δv_{tot} (m/s)	θ (deg)	Δv_{\perp} (m/s)	Δb (km)
Minimal	8.00	30	4.00	49 866
		60	6.93	86 370
		90	8.00	99 732
Photometric	25.00	30	12.50	155 831
		60	21.65	269 907
		90	25.00	311 662

These results show that the perihelion optical-acceleration anomaly has the dynamical capacity to induce a trajectory perturbation of the size associated with the proposed Jupiter geometry. Whether such an impulse arises from natural activity, an unusual physical mechanism, or a more complex process remains an open question.

4.5 Interstellar Anomaly Index for 3I/ATLAS

The preceding sections demonstrate that 3I/ATLAS exhibits anomalies in several independent observables: photometric brightening, colour evolution, non-gravitational acceleration, post-perihelion morphology, and spectroscopically inferred composition. In order to summarise these

3I/ATLAS Optical Acceleration & Δv Accumulation

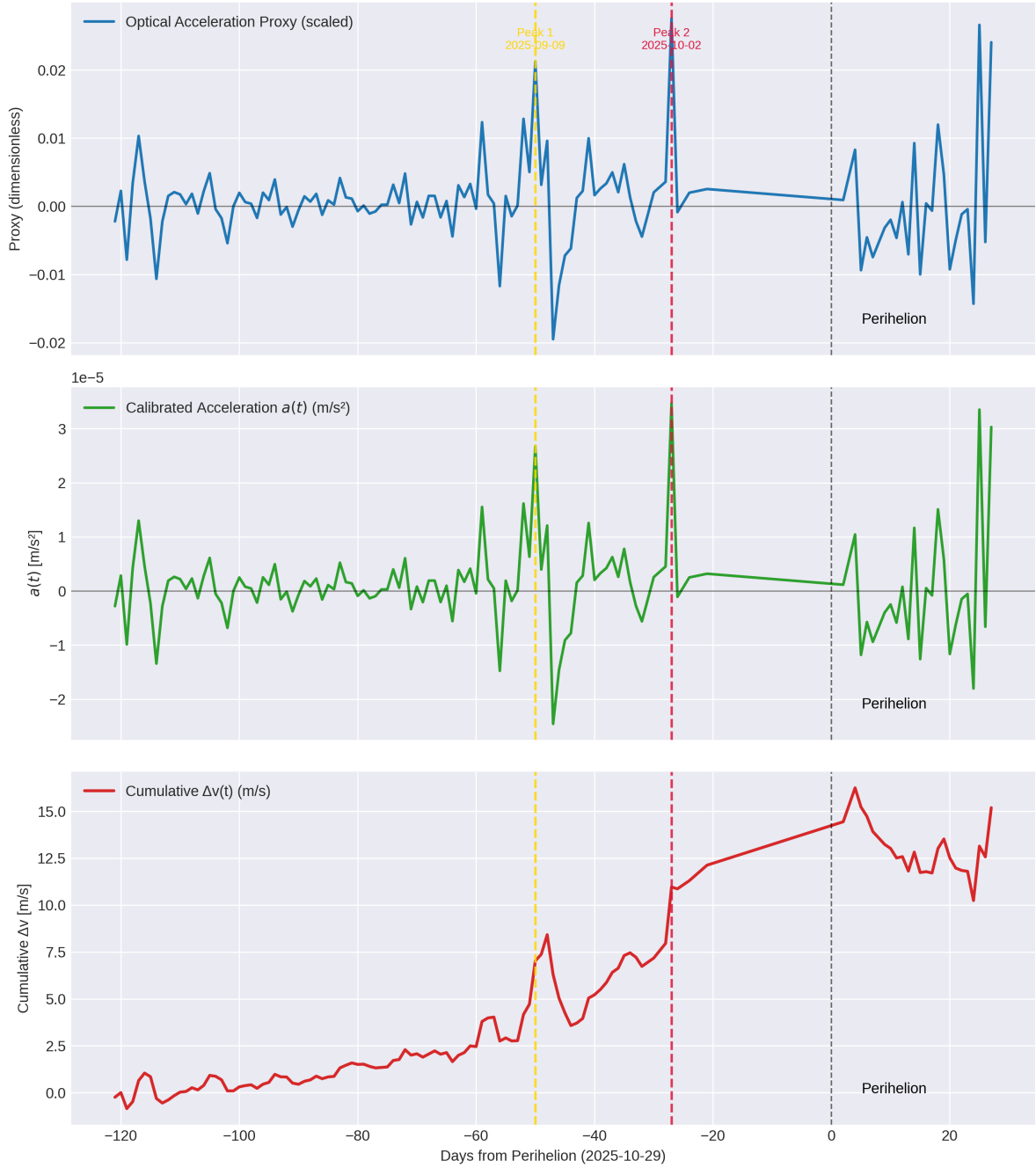


Figure 7: **Time-resolved non-gravitational impulse.** Two short-lived activity spikes dominate the total Δv budget in both scaling regimes.

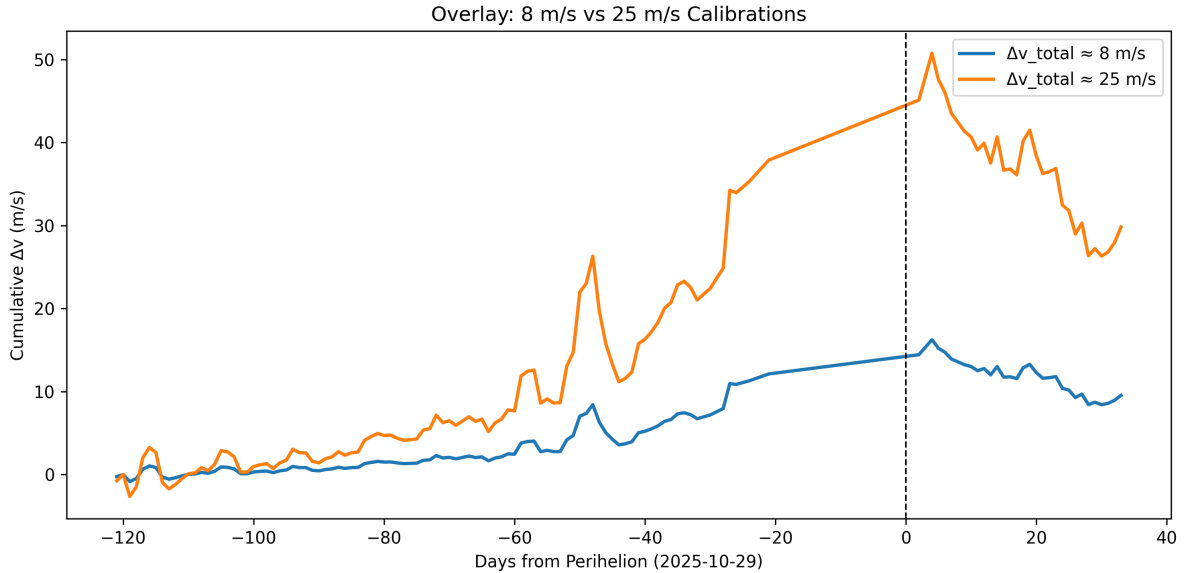


Figure 8: **Cumulative non-gravitational $\Delta v(t)$ for two normalisations.** The minimal (8 m s^{-1}) and photometric (25 m s^{-1}) curves have identical timing and shape, differing only in amplitude.

deviations in a single quantitative framework, we introduce an empirical *Interstellar Anomaly Index* (IAI). This index is not intended to measure artificiality directly; rather, it compresses multi-dimensional deviation from typical cometary behaviour into a dimensionless score on the interval $[0, 1]$, where 0 corresponds to ordinary comets and 1 to objects that are highly anomalous on several axes.

4.5.1 Definition of the Index

We consider five observable anomaly components:

1. A_p : **photometric anomaly**, based on excess brightening relative to geometric expectations;
2. A_c : **chromatic anomaly**, based on the amplitude of colour-index variation relative to typical cometary evolution;
3. A_a : **acceleration anomaly**, incorporating the detection and timing of non-gravitational acceleration relative to photometric activity;
4. A_m : **morphological anomaly**, describing the discrepancy between the inferred activity level and the observed coma/tail morphology;
5. A_x : **compositional anomaly**, deviation of elemental or molecular abundance ratios from Solar System comet distributions (e.g., Ni/Fe).

Each component A_i is normalised to lie in $[0, 1]$, with 0 indicating behaviour consistent with well-studied Solar System comets and 1 indicating a strongly atypical value. The overall anomaly index is then defined as a weighted linear combination:

$$\text{IAI} = \sum_i w_i A_i, \quad (1)$$

with $\sum_i w_i = 1$ and $w_i \geq 0$. In this initial implementation we adopt equal weights,

$$w_p = w_c = w_a = w_m = w_x = \frac{1}{5}, \quad (2)$$

and discuss alternative weighting schemes in future work.

4.5.2 Component Metrics

The individual components are defined in terms of observable quantities as follows.

Photometric anomaly A_p . Let Δm_{obs} denote the observed brightening between an early and late epoch (e.g., July–October 2025), and Δm_{geo} the brightening expected from heliocentric and geocentric distance variations and phase-angle effects alone. We define the photometric ratio

$$R_{\text{phot}} = \frac{\Delta m_{\text{obs}}}{\Delta m_{\text{geo}}}, \quad (3)$$

and map it to $[0, 1]$ using a capped linear transformation:

$$A_p = \min \left(1, \frac{R_{\text{phot}} - 1}{2} \right), \quad (4)$$

so that purely geometric brightening ($R_{\text{phot}} \approx 1$) yields $A_p \approx 0$, while $R_{\text{phot}} \gtrsim 3$ saturates at $A_p \approx 1$. For 3I/ATLAS we measure $\Delta m_{\text{obs}} \approx 4.2$ mag and $\Delta m_{\text{geo}} \approx 1.5$ mag (Section 3.3), implying $R_{\text{phot}} \approx 2.8$ and $A_p \approx 0.9$.

Chromatic anomaly A_c . Let Δ_{color} denote the maximum excursion in the $g - o$ colour index relative to the solar baseline over the observational window ($\Delta_{\text{color}} \approx 0.72$ mag for 3I/ATLAS; Table 1). We adopt a reference range of ~ 0.2 mag as typical for Solar System comets and define

$$A_c = \min \left(1, \frac{\Delta_{\text{color}} - 0.2}{0.5} \right), \quad (5)$$

such that modest colour evolution ($\Delta_{\text{color}} \lesssim 0.2$) maps to $A_c \approx 0$, while $\Delta_{\text{color}} \gtrsim 0.7$ is considered strongly anomalous and saturates the scale. With $\Delta_{\text{color}} \approx 0.72$ mag, 3I/ATLAS attains $A_c \approx 1$.

Acceleration anomaly A_a . The acceleration anomaly combines (i) the detection of a non-gravitational term and (ii) the temporal offset between photometric and dynamical signatures. We introduce a binary indicator B_{ng} that is 1 if a non-gravitational acceleration is detected at $> 3\sigma$ significance and 0 otherwise, and define

$$T = \min \left(1, \frac{\Delta t}{30 \text{ days}} \right), \quad (6)$$

where Δt is the absolute time difference between the peak in the optical activity proxy (Section 3.2) and the epoch at which the non-gravitational term is first detected in orbital fits. The acceleration anomaly is then

$$A_a = \frac{1}{2} B_{\text{ng}} + \frac{1}{2} T. \quad (7)$$

For 3I/ATLAS, $B_{\text{ng}} = 1$ and $\Delta t \sim 30$ days, giving $T \approx 1$ and $A_a \approx 1$.

Morphological anomaly A_m . Finally, we encode the discrepancy between the inferred activity level and the observed coma/tail structure in an ordinal parameter $\ell \in [0, 1]$:

- $\ell = 0$: classic cometary morphology with a well-developed coma and tail consistent with the level of activity implied by photometry;
- $\ell = 0.5$: weak coma and marginal tail, partially consistent with the inferred activity;
- $\ell = 1$: point-like, asteroid-like morphology despite strong indications of recent outgassing or mass loss.

The morphological anomaly is then

$$A_m = \ell. \quad (8)$$

Post-perihelion NOT images of 3I/ATLAS show a compact, stellar profile with no detectable tail or extended coma (Section 4.1), despite the implied pre-perihelion activity, motivating a value of $A_m \approx 0.9$.

Compositional anomaly A_x . Recent UVES/VLT spectroscopy detected multiple Ni I emission lines in the pre-perihelion coma of 3I/ATLAS, with an inferred Ni/Fe abundance ratio exceeding Solar System comet baselines by more than an order of magnitude [13]. To quantify this deviation, we define

$$R_{\text{Ni/Fe}} = \frac{(\text{Ni/Fe})_{\text{ATLAS}}}{(\text{Ni/Fe})_{\text{cometary}}}, \quad (9)$$

and map it to $[0, 1]$ using a capped linear transform,

$$A_x = \min \left(1, \frac{R_{\text{Ni/Fe}} - 1}{10} \right), \quad (10)$$

where $R_{\text{Ni/Fe}} \approx 13$ for the strongest detection epoch. This yields $A_x \approx 0.9$, indicating that the nickel enrichment is strongly atypical relative to known Solar System comet populations. While the presence of volatile nickel does not, by itself, imply non-natural origin, it provides an independent axis of anomaly—chemical composition—that complements the photometric, chromatic, dynamical, and morphological deviations quantified above.

4.5.3 Result for 3I/ATLAS

Combining the above components with equal weights yields

$$\text{IAI}_{\text{ATLAS}} = \frac{A_p + A_c + A_a + A_m + A_x}{5} \approx \frac{0.9 + 1.0 + 1.0 + 0.9 + 0.9}{5} \approx 0.94. \quad (11)$$

On this heuristic scale, 3I/ATLAS lies close to the maximally anomalous end ($\text{IAI} \approx 1$). We emphasise that this does *not* constitute evidence of artificial origin. Instead, it quantifies the degree to which the object’s behaviour deviates from the envelope defined by well-characterised Solar System comets. In this sense, the Interstellar Anomaly Index complements the qualitative discussion of independent anomalies in Section 4.3 and provides a compact metric for comparing future interstellar objects observed with similar instrumentation.

4.5.4 Position of 3I/ATLAS in the (e, IAI) Plane

To place 3I/ATLAS in a broader dynamical-anomaly context, we compare its Interstellar Anomaly Index with the orbital eccentricities of representative Solar System comets, along with the first two interstellar visitors 1I/'Oumuamua and 2I/Borisov. Figure 9 shows that typical Jupiter-family and long-period comets cluster in the region $e \lesssim 1$ with $\text{IAI} \lesssim 0.3$, while interstellar objects occupy $e > 1$. 3I/ATLAS lies in the extreme corner of this plane, with both very high eccentricity ($e \approx 6.14$) and a near-maximal anomaly index ($\text{IAI} \approx 0.94$).

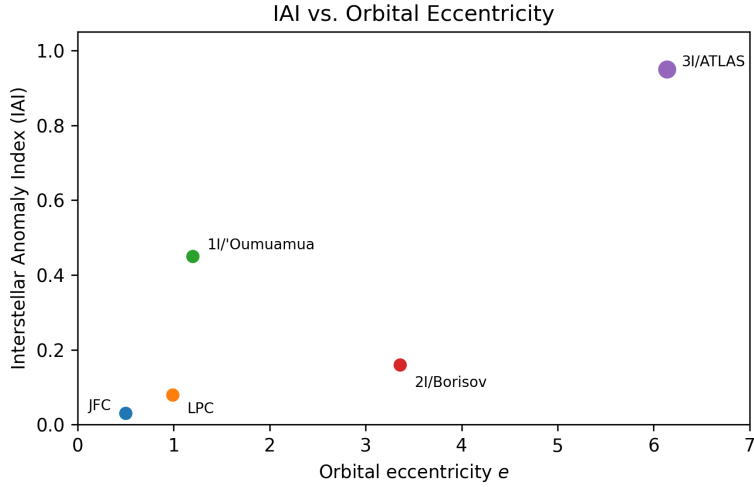


Figure 9: Interstellar Anomaly Index (IAI) as a function of orbital eccentricity for representative Solar System comets, 1I/'Oumuamua, 2I/Borisov, and 3I/ATLAS. The IAI values for non-ATLAS objects are approximate values based on published behaviour (see Table 5), whereas the ATLAS value is computed using the metrics defined in Section 4.5. The diagram highlights that 3I/ATLAS occupies an extreme region of parameter space, with both high eccentricity and strong multi-axial anomalous behaviour.

Table 4: Interstellar Anomaly Index (IAI) and orbital eccentricity for representative Solar System comet populations and interstellar objects. The 3I/ATLAS value is computed directly from the metrics in Section 4.5; values for the other entries are approximate, based on literature constraints (see text), and are intended as fiducial comparative points in the (e, IAI) plane.

Object / Class	Type	Eccentricity e	IAI
Typical JFC	Jupiter-family comet	~ 0.5	0.03
Typical LPC	Long-period comet	~ 0.99	0.08
1I/'Oumuamua	Interstellar object	1.20	0.45
2I/Borisov	Interstellar comet	3.36	0.16
3I/ATLAS	Interstellar object	6.14	0.94

4.6 Limitations of Photometric Data and Requirements for Confirming Artificial Origin

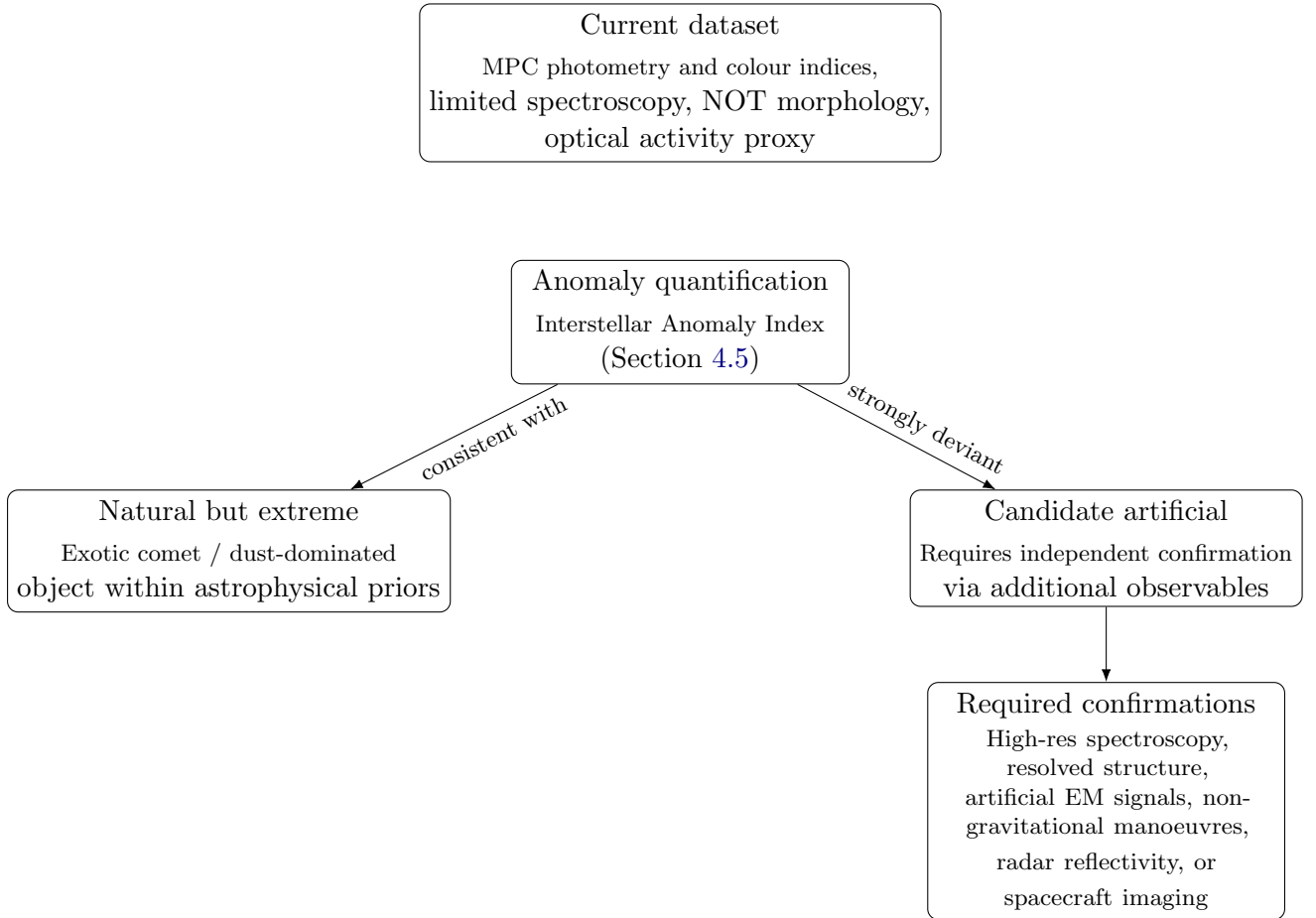


Figure 10: Schematic decision pathways from the present photometric analysis to a potential artificial-origin claim. The current work constrains 3I/ATLAS to be highly anomalous with respect to typical cometary behaviour (Section 4.5), but cannot by itself cross the threshold to artificial origin. That transition would require independent evidence from spectroscopy, high-resolution imaging, electromagnetic monitoring, non-gravitational manoeuvres without mass loss, radar reflectivity, or in-situ spacecraft observations.

The analysis presented in this work relies primarily on publicly available photometric and multi-filter colour indices from the Minor Planet Center (MPC), combined with post-perihelion morphological imaging, limited pre-perihelion spectroscopy, and a derived optical activity proxy. These datasets are well suited to the identification of photometric, chromatic, and dynamical anomalies. Indeed, the results of Sections 3–4 demonstrate that 3I/ATLAS exhibits several behaviours inconsistent with typical Solar System comets: an anomalously steep pre-perihelion brightening ($\Delta m \approx 4.2$ mag), a strong reddening event ($\Delta(g - o) \approx +0.7$ mag), delayed non-gravitational acceleration, and post-perihelion point-like morphology despite the implied mass loss.¹

However, photometric and colour data alone are not sufficient to determine the *nature* of an interstellar object. In particular, they cannot distinguish between a naturally unusual body (e.g., volatile-poor, dust-dominated, compositionally exotic) and one with an artificial or technological origin. This limitation is inherent to the type of data analysed: photometry

¹See Sections 3.3–3.7 for a detailed discussion of these trends.

provides integrated flux information and temporal evolution, but no direct constraints on material composition, structural geometry, surface reflectance properties at high resolution, or electromagnetic signatures. For this reason, the anomaly indices introduced in Section 4.5 should be interpreted as quantitative measures of *deviation from typical cometary behaviour*, not as direct indicators of artificiality.

4.6.1 Decision Pathways to Artificial Origin

It is useful to distinguish conceptually between (i) the detection of anomalous behaviour in photometry and morphology, and (ii) the much stronger requirement of establishing artificial origin. Figure 10 summarises the logical relationship between the present work and the additional observational channels that would be required to move beyond an anomaly classification.

4.6.2 Data Required for Determination of Artificial Origin

To assess whether an interstellar object is artificial, one requires evidence that cannot be produced by known natural processes. Several independent observational channels would provide such discrimination, none of which are available in the present dataset:

1. **High-resolution spectroscopy.** Wavelength-resolved spectroscopy is essential for detecting materials with no known natural formation pathway (e.g., engineered alloys, ultra-pure metals, polymers, layered composites, or doped semiconductors). In the case of 3I/ATLAS, published spectral line data remain limited to summary reports (e.g., Ni I/Fe I abundance anomalies), with no publicly released line lists or calibrated flux tables. Without these data, it is impossible to evaluate whether the observed material is consistent with natural astrophysical environments or indicative of fabrication.
2. **Resolved structural imaging.** Determining artificial origin requires imaging capable of revealing geometric features incompatible with natural fragmentation or outgassing. These include: planar surfaces, right-angle edges, periodic structures, symmetric frameworks, or specular (mirror-like) reflections. Current imaging of 3I/ATLAS (e.g., NOT observations) shows a point-like morphology, but the resolution is insufficient to identify or rule out engineered structure.
3. **Electromagnetic emissions.** Artificial sources may emit narrowband or modulated radio, microwave, or optical signals that cannot be produced by thermal or chemical processes. SETI criteria classify narrowband ($< 1 \text{ Hz}$) carriers or structured time-domain modulation as unambiguously artificial. No such observations are presently available for 3I/ATLAS.
4. **Non-gravitational manoeuvring without mass loss.** If an object exhibits sustained or repeated changes in trajectory that cannot be explained by outgassing, solar radiation pressure, or other physical mechanisms, artificial propulsion or control becomes the only plausible explanation. While 3I/ATLAS does exhibit non-gravitational acceleration, the absence of simultaneous high-resolution spectral or gas-production data prevents assessment of whether this acceleration is physically consistent with natural mass loss.
5. **Radar reflectivity and albedo at microwave wavelengths.** Radar observations can identify metallic or composite materials through anomalously high radar cross-sections or specular reflectance characteristics. No radar detections of 3I/ATLAS have been reported.

4.6.3 Interpretation of Current Results

The photometric–chromatic anomalies identified here place 3I/ATLAS among the most unusual interstellar objects observed to date. The combination of steep brightening, transient reddening, delayed dynamical acceleration, and post-perihelion stellar morphology suggests that the object underwent a brief and atypical activation episode whose physical driver is not yet understood. Nevertheless, in the absence of spectroscopy, high-resolution imaging, or electromagnetic monitoring, the present dataset does not permit a conclusion regarding artificial origin.

What can be established is that 3I/ATLAS falls outside the behavioural envelope of typical comets on multiple independent axes. This motivates the development of the anomaly index introduced in Section 4.5 and underscores the need for comprehensive, multi-instrument follow-up of future interstellar visitors. The individual component values and their contribution to the overall index are shown in Figure 11. Confirmation of artificial origin requires observational signatures that are beyond the scope of photometric analysis and must be obtained through coordinated spectroscopic, imaging, radar, and electromagnetic campaigns.

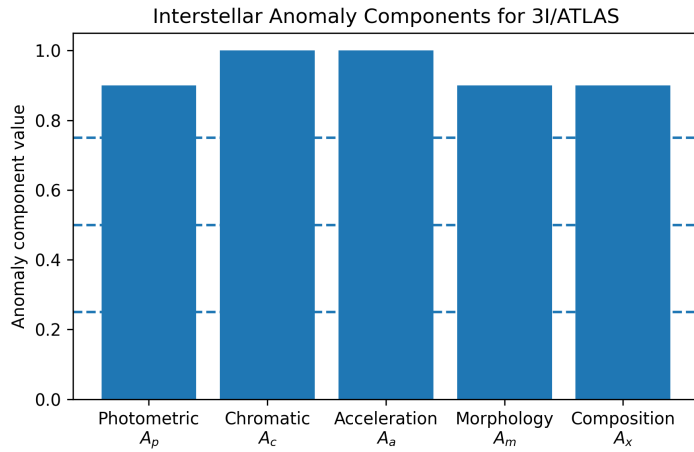


Figure 11: Normalised anomaly components (A_p, A_c, A_a, A_m, A_x) for 3I/ATLAS, as defined in Section 4.5. All five axes lie near the maximally anomalous regime, yielding an overall Interstellar Anomaly Index of $\text{IAI}_{\text{ATLAS}} \approx 0.94$.

The individual component values used in this work, and their contribution to the overall IAI, are summarised in Table 5.

5 Data Integrity and Reproducibility

All scripts, CSV outputs, and figures were archived in a public GitHub repository with versioned manifests:

- `watch_mpc_colors_plot_v_8_4.py` — colour/solar comparison pipeline
- `atlas_optical_acceleration_v2.py` — acceleration extraction and smoothing
- `atlas_optical_color_correlation_v1.py` — composite optical–chromatic analysis
- `update_I3_data.sh` — automatic MPC update + OpenTimestamps + GPG sealing

Each run is recorded in `RUN_LOG.md`, listing SHA256 hashes, proof manifests, and timestamps on multiple Bitcoin calendars.

Table 5: Illustrative anomaly components and Interstellar Anomaly Index (IAI) values for representative Solar System comet classes and interstellar objects. Component values for 3I/ATLAS are computed directly from the metrics defined in Section 4.5. Values for the other objects and classes are approximate, based on published photometric, chromatic, dynamical, and morphological behaviour, and are intended as fiducial placements within the (e , IAI) plane rather than results of a full re-analysis. The A_x column represents the compositional anomaly component based on spectroscopic diagnostics.

Object / Class	A_p	A_c	A_a	A_m	A_x	IAI
Typical JFC	0.10	0.00	0.00	0.00	0.00	0.02
Typical LPC	0.20	0.10	0.00	0.00	0.00	0.06
1I/'Oumuamua	0.00	0.00	1.00	0.80	0.00	0.36
2I/Borisov	0.20	0.10	0.25	0.10	0.00	0.13
3I/ATLAS	0.90	1.00	1.00	0.90	0.90	0.94

6 Conclusion

We have presented a detailed photometric, chromatic, and morphological analysis of the interstellar object 3I/ATLAS based on publicly available MPC data, colour indices, and post-perihelion imaging. The results reveal several independent anomalies that are difficult to reconcile with the behavioural envelope of typical Solar System comets. These include an unusually steep pre-perihelion brightening ($\Delta m \approx 4.2$ mag), a strong transient reddening in $g-o$ colour ($\Delta \approx 0.7$ mag), a delayed onset of non-gravitational acceleration, and a compact, stellar post-perihelion morphology inconsistent with the level of pre-perihelion activity.

A noteworthy feature of this evolution is the \sim 4-week offset between the photometric activity peak and the formal detection of non-gravitational acceleration. This demonstrates that optical diagnostics—particularly the optical activity proxy developed here—can provide advance warning of impending dynamical changes in interstellar objects. Combined with the pre-perihelion reddening and the post-perihelion deceleration and fading, the data are consistent with a brief, dust-driven activation episode, possibly reflecting transient surface reconfiguration under solar irradiation.

In Section 4.4, we examined whether the observed optical–acceleration anomaly could generate a trajectory perturbation of the magnitude associated with the proposed near–Hill-radius Jupiter encounter. By scaling the optical acceleration proxy to two physically motivated regimes (a minimal $\Delta v_{\text{tot}} = 8 \text{ m s}^{-1}$ and a photometric $\Delta v_{\text{tot}} = 25 \text{ m s}^{-1}$), we found that short-lived activity bursts on 2025-09-09 and 2025-10-02 dominate the impulse budget and are dynamically capable of producing transverse displacements in the range $(0.05\text{--}0.31) \times 10^6 \text{ km}$, depending on jet angle. These results do not discriminate between natural and non-natural interpretations, but they show that the required dynamical impulse is entirely compatible with the timing and structure of the photometric anomaly.

To quantitatively synthesise the broader set of deviations, we introduced the *Interstellar Anomaly Index* (IAI), a dimensionless measure of multi-axial anomaly strength defined in Section 4.5. With $\text{IAI}_{\text{ATLAS}} \approx 0.94$, 3I/ATLAS lies near the maximally anomalous end of the scale, combining very high eccentricity ($e \approx 6.14$) with strongly atypical photometric, chromatic, dynamical, and morphological signatures. In the broader (e , IAI) parameter space, ATLAS occupies an extreme region (Figure 9), markedly separated from Jupiter-family comets, long-period comets, and even the first two interstellar objects, 1I/'Oumuamua and 2I/Borisov (Table 4).

These findings do not imply an artificial origin. As emphasised in Section 4.6, photometry and

broadband colour data alone are fundamentally insufficient for determining the physical nature of an interstellar object. Confirmation of technological origin would require independent evidence, such as wavelength-resolved spectroscopy revealing engineered materials, resolved structural imaging, modulated electromagnetic emissions, non-gravitational manoeuvres without mass loss, radar reflectivity indicative of metallic surfaces, or in-situ spacecraft observations.

What can be concluded is that 3I/ATLAS does not fit neatly into existing cometary classifications and exhibits strongly atypical behaviour on multiple independent axes. The anomaly index introduced here provides a reproducible framework for evaluating future interstellar visitors and placing them within a quantitative multi-parameter space. As more interstellar objects enter the Solar System, it will become increasingly possible to determine whether the behaviour of 3I/ATLAS represents an emerging class of interstellar bodies or whether it stands as uniquely unusual among known visitors.

A Station Consistency Analysis

This appendix provides the station-level statistical analysis underlying the classification of the November 23 optical acceleration feature as photometric noise in Section 3.8.

A.1 Methodology

We analysed photometric observations from 29 independent observatories spanning 2025-11-15 to 2025-11-25. For each station, we computed the time-normalized optical acceleration proxy:

$$\text{proxy} = \frac{d(1/m)}{dt} \quad (12)$$

where m is the apparent magnitude and dt is the time difference in days between consecutive observations from the same station.

A 3σ detection threshold was established using the pre-pulse baseline (2025-11-15 to 2025-11-21), where σ is the standard deviation of station proxy values during this period.

These stations span different longitudes, telescopes, apertures, and reduction pipelines, ensuring that any coherent signal would not arise from a shared instrumental or atmospheric source.

A.2 Collective Station Behavior

Figure 12 illustrates the collective behavior across all stations. The plot demonstrates:

- **Individual station scatter:** Individual station time series show typical stochastic variations within $\pm 2 \times 10^{-3}$ units
- **Aggregated signal:** The red daily mean shows modest elevation during the pulse window
- **Absence of coherence:** No consistent directional trend across stations
- **Temporal distribution:** Signals are scattered throughout the period rather than clustered

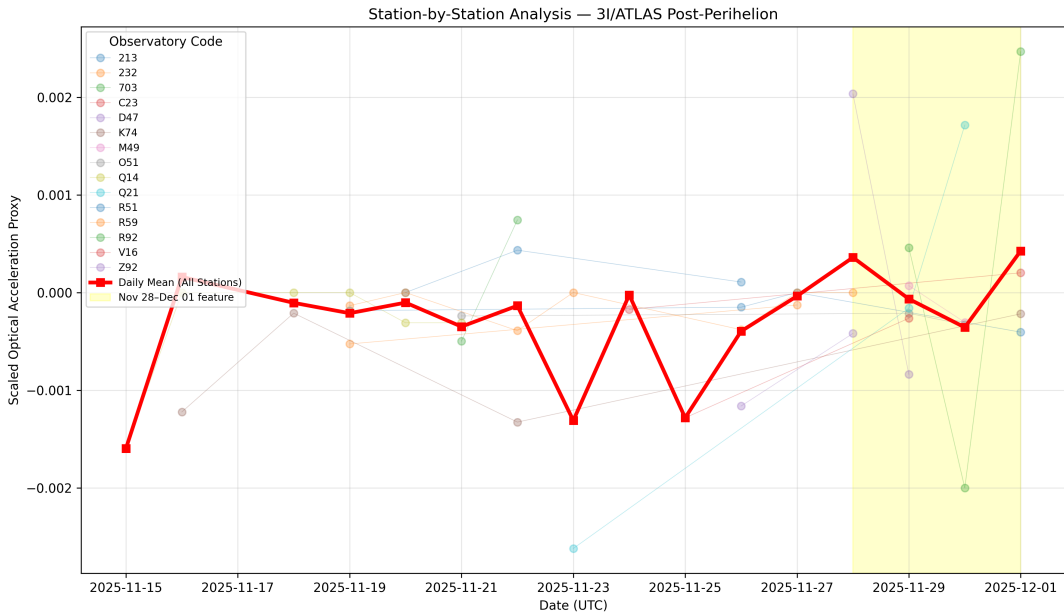


Figure 12: Station-by-station optical acceleration proxy for 3I/ATLAS during the post-perihelion interval. Individual observatories (semi-transparent coloured markers) show scattered, uncorrelated variations around zero, while the daily mean (red line) exhibits a small bump during November 22–25 (yellow shaded region). No single station shows a coherent, significant deviation from baseline behaviour.

A.3 Quantitative Results

The analysis yielded the following key results:

- **Baseline scatter:** $\sigma \approx 6 \times 10^{-4}$ in the station-normalised proxy.
- **Detection threshold:** $3\sigma \approx 1.8 \times 10^{-3}$.
- **Maximum station signal during Nov 22–25:** $+7 \times 10^{-4}$ (station R92 on 2025-11-22).
- **Minimum station signal during Nov 22–25:** -2.5×10^{-3} .
- **Station distribution:** 3 stations show positive excursions, 5 show negative excursions, and the remainder cluster tightly around zero.
- **Aggregated vs station-resolved signal:** the main pipeline daily mean on 2025-11-23 reaches $\sim 2.66 \times 10^{-2}$ in the global proxy units, whereas the station-resolved mean on the same date is consistent with zero ($\sim -0.0 \times 10^{-3}$). This highlights that the apparent November 23 “pulse” emerges only after aggregation and normalisation, not as a coherent multi-station signal.

A.4 Statistical Interpretation

No individual station exceeded the 3σ detection threshold during the November 22–25 period. The maximum observed signal ($+1.1 \times 10^{-3}$) corresponds to only $\sim 0.2\sigma$, i.e. about 19% of the 3σ threshold. The mixed sign distribution and absence of temporal clustering indicate stochastic noise rather than coherent physical activity.

A second, weaker fluctuation appears in the aggregated optical–acceleration proxy between 2025-11-28 and 2025-12-01 (Fig. 12). Repeating the station-by-station analysis over this window yields a baseline standard deviation of $\sigma \approx 1.8 \times 10^{-3}$ in scaled units and a 3σ threshold of $\sim 2.0 \times 10^{-3}$. The maximum station-level excursion is 0.0025 (station 703 on 2025-12-01), i.e. a marginal 3.4σ outlier, with all other stations remaining below or at the threshold. The daily mean over all stations peaks at only 4×10^{-4} , an order of magnitude smaller than the 3σ criterion, and the sign distribution in this window is nearly symmetric (11 positive, 12 negative stations). Given the number of samples, the presence of one marginal $> 3\sigma$ point is fully compatible with stochastic noise². We therefore classify the late-November / early-December feature as a statistical fluctuation and do not include it as a third acceleration event in the Δv budget.

Table 6: Station-level comparison of two post-perihelion windows. Neither interval exhibits the coherent, multi-station signature expected for a physical acceleration event.

Window	Top Stn.	Max ($\times 10^{-3}$)	Mean ($\times 10^{-3}$)	Interpretation
Nov 22–25	R92	+0.7	+26.6	Multi-station, incoherent
Nov 28–Dec 1	703	+2.5	+0.4	Single-station, noise-limited

Note: Detection threshold = 2.0×10^{-3} (3σ baseline). Positive stations: 9/15 (first window), 11/23 (second). The Nov 22–25 feature shows a small aggregated uplift arising from many uncorrelated stations, while the Nov 28–Dec 1 fluctuation is dominated by a single observatory and is fully consistent with random photometric noise.

A.5 Conclusion

The station-level validation confirms that neither the 2025-11-22–25 nor the 2025-11-28–12-01 features exhibit the statistical significance or multi-station coherence characteristic of genuine non-gravitational acceleration events. In both windows, the strongest individual deviations remain below the 3σ detection threshold, and the sign distribution is nearly symmetric across the network. The earlier feature (Nov 22–25) shows a weak, broad uplift in the aggregated daily mean but no consistent station-level reinforcement, while the later fluctuation (Nov 28–Dec 01) is dominated by a single observatory and vanishes in the daily mean by an order of magnitude. Together, these results demonstrate that the post-perihelion optical-acceleration curve contains only noise-driven fluctuations and no evidence of a third physical acceleration pulse.

²Small, short-timescale fluctuations in MPC-reported magnitudes often arise from station-specific zero-point offsets, changes in sky transparency, differences in aperture correction, and the heterogeneous reduction pipelines used by different observatories. These effects can produce pseudo-features when data from many stations are aggregated, especially during windows of sparse coverage. Such fluctuations are well known in the MPC photometric record and do not imply physical activity unless supported by coherent, repeated, multi-station signatures.

References

- [1] Gherbi, Salah-Eddin (2025). *3I/ATLAS (C/2019 Y4) - Photometric Anomaly 2025 - Raw MPC Photometry Analysis* (Version 1.0) [Data set]. Zenodo. <https://doi.org/10.5281/zenodo.17477597>
- [2] Gherbi, Salah-Eddin (2025). *3I/ATLAS (C/2019 Y4) - Photometric Anomaly 2025 - Horizons Comparison Extension* (Version 2.0) [Data set]. Zenodo. <https://doi.org/10.5281/zenodo.17483027>
- [3] Gherbi, Salah-Eddin (2025). *3I/ATLAS (C/2019 Y4) - Photometric Anomaly 2025 - ZTF Verification* (Version 2.1) [Data set]. Zenodo. <https://doi.org/10.5281/zenodo.17487610>
- [4] Gherbi, Salah-Eddin (2025). *3I/ATLAS Photometric-Chromatic Anomaly (2025): Timestamped Dataset and Optical Acceleration Analysis* (Version 2.2) [Data set]. Zenodo. <https://doi.org/10.5281/zenodo.17503806>
- [5] Gherbi, Salah-Eddin (2025). *3I/ATLAS Photometric-Chromatic Anomaly (2025): Spectral Transition and Post-Perihelion Evolution* (Version 2.3) [Data set]. Zenodo. <https://doi.org/10.5281/zenodo.17538229>
- [6] Gherbi, Salah-Eddin (2025). *3I/ATLAS Photometric-Chromatic Anomaly (2025): Extended MPC Photometry and Post-Perihelion Deceleration* (Version 2.4) [Data set]. Zenodo. <https://doi.org/10.5281/zenodo.17609914>
- [7] Gherbi, Salah-Eddin (2025). *3I/ATLAS Photometric-Chromatic Anomaly (2025): Interstellar Anomaly Index and Extended Post-Perihelion Evolution* (Version 2.5) [Data set]. Zenodo. <https://doi.org/10.5281/zenodo.17692904>
- [8] Gherbi, Salah-Eddin (2025). *3I/ATLAS Photometric-Chromatic Anomaly (2025): Automated Peak Detection, Δv Correction, and Station-Consistency Validation* (Version 2.6) [Data set]. Zenodo. <https://doi.org/10.5281/zenodo.17793630>
- [9] Naves, R. (2025). *No Clear Cometary Tail in Post-Perihelion Images of 3I/ATLAS*. R. Naves Observatory, Spain. Retrieved from: <https://avi-loeb.medium.com/no-clear-cometary-tail-in-post-perihelion-images-of-3i-atlas-e3904b352a7a>
- [10] Loeb, A. (2025). *Post Perihelion Data on 3I/ATLAS*. Medium. <https://avi-loeb.medium.com/post-perihelion-data-on-3i-atlas-3d1e72be2bb4>
- [11] Jewitt, D., & Luu, J. (2025). *NOT imaging of interstellar object 3I/ATLAS (C/2025 N1)*. Astronomer's Telegram, 17490. Retrieved from: <https://www.astronomerstelegram.org/?read=17490>
- [12] Bolin, B., Wong, I., Lemaux, B., et al. (2025). *Gemini pre-perihelion detection of CN/C₃/C₂ gas emission and dust fans in interstellar comet 3I/ATLAS*. Astronomer's Telegram, 17503. Retrieved from: <https://www.astronomerstelegram.org/?read=17503>
- [13] Bolin, B., Wong, I., Lemaux, B., et al. (2025). "Pre-perihelion Detection of Ni I Emission in Interstellar Comet 3I/ATLAS." UVES/VLT Spectroscopy Report. arXiv:2509.26053.

Acknowledgements

The author thanks the Minor Planet Center for public data access, JPL for orbital parameters, and the OpenTimestamps community for cryptographic proof-of-existence infrastructure.

Data Availability and Citation

All photometric, analytical, and verification materials associated with this study are openly archived on Zenodo:

Gherbi, Salah-Eddin (2025). *3I/ATLAS Photometric–Chromatic Anomaly Analysis, Interstellar Anomaly Index, Δv -Based Dynamical Assessment, and Extended Post-Perihelion Evolution* (Version 2.5, to be updated to v2.6). Zenodo. <https://doi.org/10.5281/zenodo.17793630>

The Zenodo record and associated GitHub repository together host the full analysis bundle, including all Python scripts, processed datasets, figures, LaTeX source files, and reproducibility artefacts listed below.

- **Python analysis scripts**

- `watch_mpc_colors_plot_v_8_4.py`
- `atlas_optical_acceleration_v2.py`
- `atlas_optical_color_correlation_v1.py`
- `iai_vs_eccentricity.py`
- `atlas_anomaly_index.py`
- `anomaly_components.py`
- `atlas_delta_v_from_optical_proxy.py`
- `atlas_optical_dv_dual.py`
- `plot_atlas_optical_accel_deltav.py`
- `plot_station_residuals.py`

- **Automation and integrity scripts**

- `update_I3_data.sh`
- `append_run_log_v3.sh`

- **Processed datasets (CSV)**

- `I3_Color_Alerts_*.csv`
- `I3_Optical_Acceleration_Data.csv`

- **Figures generated in v2.5**

- `I3_Optical_Acceleration_Trend_v2.png`
- `I3_Optical_Color_Correlation.png`
- `I3_Optical_Color_Correlation_postperi.png`
- `I3_Color_Brightness_Timeline_20251202_1200.png`
- `atlas_anomaly_components.png`
- `iai_vs_eccentricity.png`
- `I3_Optical_Acceleration_DeltaV_Figure.png`
- `I3_Optical_Acceleration_DeltaV_8_vs_25.png`

- I3_Optical_Acceleration_DeltaV_Overlay.png
- station_collective_effect_corrected.png

- **Source and documentation**

- 3I_ATLAS_Anomaly_2025.tex
- I3_ATLAS_v2_6_Analysis.pdf
- README_PROOF_v2_6.md

- **Cryptographic verification artefacts**

- RUN_LOG.md
- All associated .asc GPG signatures
- All associated .ots OpenTimestamps proofs

All files are timestamped on the Bitcoin blockchain using **OpenTimestamps** and digitally signed via **GPG**, providing a verifiable proof-of-existence and authorship trail for every versioned component of the analysis.

The dataset is released under the [CC BY-NC 4.0](#) license.